Natural Decadal Variability of Antarctic Sea Ice Modulated by Mesoscale Ocean Memory

Qian Li[a,c,1] **and John Marshall**[a,b]

This manuscript was compiled on March 31, 2025

Antarctic sea ice extent (SIE) exhibits low-frequency variability, having experienced decades of record highs followed by a pronounced decadal decline. The causes of these changes, whether driven by internal climate variability or external anthropogenic forcings, continue to be debated. Guided by theory of the ocean's meridional overturning circulation, we investigate mechanisms of decadal changes in Antarctic SIE using a fully coupled climate model, focusing on the role of the ocean's mesoscale in transporting heat into the seasonal sea ice zone and thereby modulating its ice edge. The essentially white-noise external forcing by predominantly zonal winds leads to high-frequency fluctuations of the Ekman component of the overturning cell. The eddy-driven component, instead, responds on decadal timescales — set by mesoscale eddy-compensation dynamics — leading to decadal modulation in meridional heat transport and SIE. A stochastic (Hasselmann-like) model is developed and guides analysis of the climate model, in which the damping timescale is set by mesoscale eddy adjustment. This provides a null hypothesis from which to contemplate the recent observed decadal decline in Antarctic sea ice: it may be part of a natural cycle and not necessarily or entirely associated with anthropogenic climate change.

Antarctic sea ice | Ocean memory | Mesoscale eddies | Southern Ocean | Natural climate variability

Antarctic sea ice is a central element of the climate system, comprising an insulating, highly reflective icy surface which, as it expands and contracts, undergoes the largest seasonal cycle on Earth. Through its effect on albedo, air-sea heat exchange and cloud cover (1–3), it shapes regional climate, influences global air temperatures, modulates bottom water production and ocean thermohaline circulation through brine rejection (4–6), and regulates ocean carbon uptake and nutrient cycles (7–10). The seasonal expansion of Antarctic sea ice also acts as a protective buffer for ice shelves along the Antarctic coast, reducing the impact of ocean waves and stabilizing these large floating masses (11).

Despite a probable link between Arctic sea ice loss and anthropogenic global warming since the 1990s (12–14), Antarctic sea ice has experienced a gradual increase in overall extent during the satellite era, from 1979 to 2014 (15–18), followed by a sharp decline in 2016 (19–21) and a subsequent new record low in 2023 (22, 23) (Fig. 1a). This transition – some call it a "regime shift" – from decades-long expansion to contraction has generated much recent attention (24–27). The cause of the decadal variability in the extent of Antarctic sea ice (SIE), specifically the degree to which it is due to internal variability and / or external forcing (for example, due to greenhouse gases affecting surface air temperatures (28) or stratospheric ozone depletion influencing surface winds (29)), remains a topic of debate.

Antarctic sea ice has distinct characteristics, shaped by its geography, that distinguish it from Arctic sea ice. It is thinner and more expansive, particularly in winter, with a more pronounced melt from its base compared to the Arctic (30). In addition, Antarctic sea ice exhibits marked seasonal to interannual variations, mainly due to its extension to midlatitudes, where it becomes increasingly exposed to fluctuations in westerly winds and complex interactions with the underlying ocean (31–33). One might expect that Antarctic SIE undergoes low-frequency variability on decadal-to-multidecadal timescales. Previous studies using coupled climate models have suggested that the natural variability of the climate system may contribute significantly to the long-term increase observed in Antarctic SIE (34–36). Potential modulators include positive ice–ocean feedback (37), the El Niño Southern Oscillation (ENSO), the Southern Annular Mode (SAM) (38–42), the Interdecadal Pacific Oscillation (IPO) (43), and internal variability of deep convection (44). Regarding the recent decadal decline in Antarctic SIE, the mechanisms

Significance Statement

Antarctic sea ice extent has recently experienced an unprecedented decadal decline, raising questions about its underlying causes. Here, we identify ocean-driven mechanisms that modulate the extent of sea ice on decadal timescales. Mesoscale eddies, which regulate heat transport to the sea ice edge through the ocean's meridional overturning circulation, emerge as a critical driver. These findings emphasize the need to disentangle natural climate variability from anthropogenic effects to understand recent changes in Antarctic sea ice and their broader climate implications.

Author affiliations: [a]Department of Earth, Atmospheric, and Planetary Sciences, Massachusetts Institute of Technology, Cambridge, MA, USA 02139; [b]NASA Goddard Institute for Space Studies, New York, NY, USA 10025; [c]Department of Earth, Ocean, and Atmospheric Science, Florida State University, Tallahassee, FL, USA 32304

Q.L. and J.M. conceived the study, produced the analyses, and wrote the manuscript.

The authors declare no competing interests.

[1] E-mail: qian_li@mit.edu

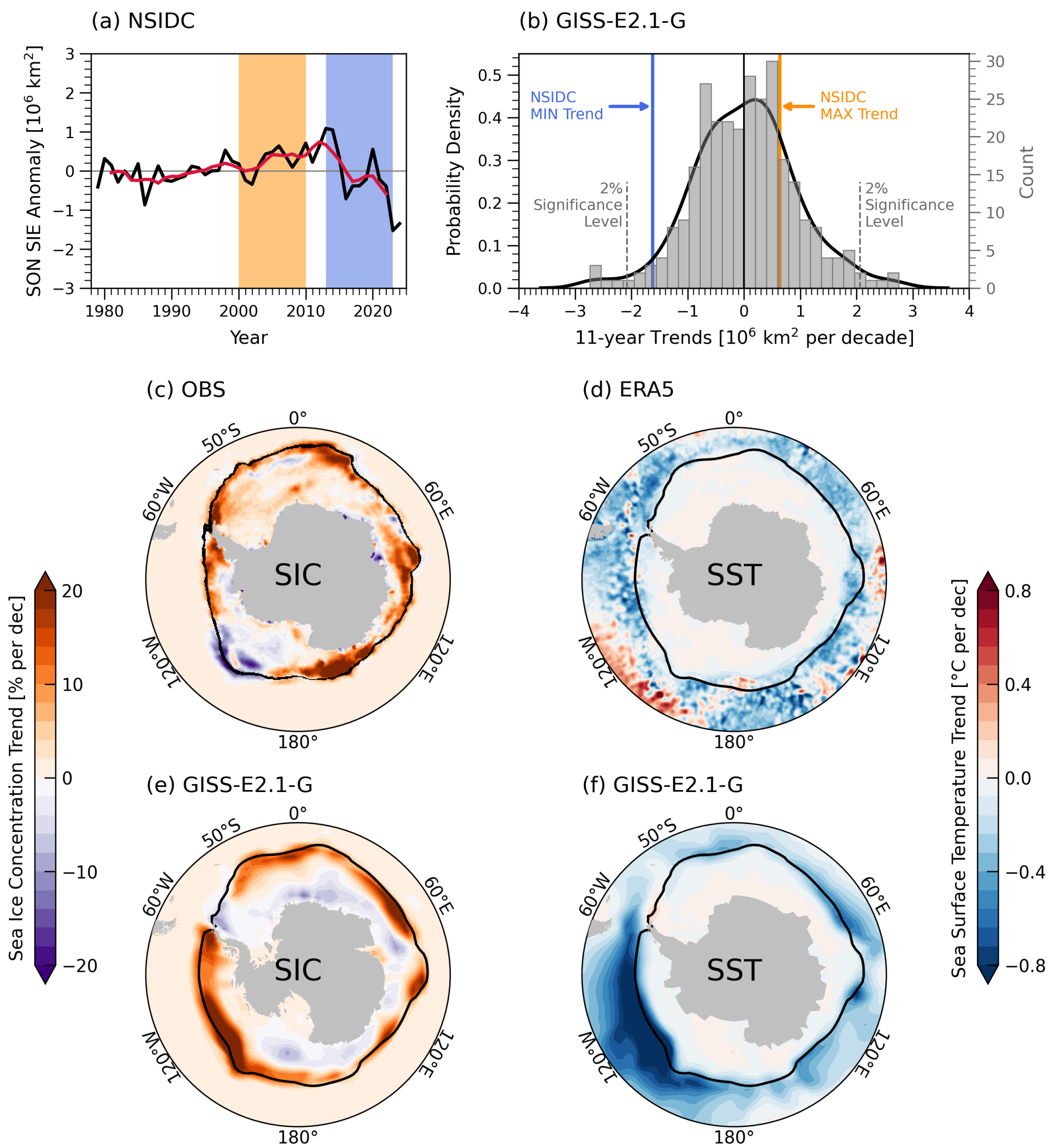

Fig. 1. Decadal trends in Antarctic sea ice and Southern Ocean SST. (a) Observed time series of spring (SON) Antarctic SIE anomalies (black line; 10^6 km^2) and its 5-year moving average (red line) from NSIDC during 1979–2024. The decadal periods of sea ice advance (2000–2010) and retreat (2013–2023) are indicated by orange and blue shadings, respectively. (b) Probability density distributions of 11-year trends in the spring Antarctic SIE from piControl of the GISS coupled climate model. The 2% significance level is indicated (dashed grey line). The observed maximum and minimum trends for 2000–2010 (solid orange line) and 2013–2020 (solid blue line), respectively. During a decadal period of sea ice advance, 11-year trends in the spring Antarctic SIC (colors; % per dec) and the Southern Ocean SST (colors; ℃ per dec) from (c) satellite observation and (d) ERA5, and from (e, f) piControl, respectively. The black contour denotes the climatological Antarctic sea-ice edge during spring.

remain unclear, perhaps because of the short and incomplete observational record. The warming of the subsurface across the Southern Ocean may perhaps gradually destabilize the upper ocean and sustain a persistent decline in SIE (26, 45). From one perspective, this subsurface warming could be caused by anthropogenic climate change (46) or enhanced westerly winds due to ozone depletion (47). In contrast, the ocean, with its enormous heat capacity, responds slowly to high frequencies, leading to "reddening" of the spectrum of climate variability (48). In this study, we argue that natural climate variability is likely a contributor to recent reductions in Antarctic SIE. Moreover, we explore and show evidence to support a possible mechanism involving the decadal modulation of mesoscale ocean heat transport to the seasonal sea ice zone.

Oceans are recognized to have a long memory due to their high thermal inertia and the long time scale of ocean circulation (49–51). In particular, fluctuations in the physical (and biogeochemical) properties of the Southern Ocean are modulated by low-frequency ocean processes, including the heat transported by meridional overturning circulation cells (MOC) (52–56). Wind-driven MOC (the Deacon Cell) responds almost instantaneously to changing zonal winds, but partially compensating eddy-driven MOC (57–59), responds on much longer multi-year timescales (60, 61). We will argue that it is this timescale, controlled by the ocean mesoscale, that plays an important role in modulating Antarctic SIE on longer timescales. For example, an early study by Hogg et al. (2008) (62) of an idealized channel model of the Antarctic Circumpolar Current (ACC) without ice suggested that increased interannual wind forcing initially cools the surface ocean, but enhanced eddy activity induces warming 3-6 years later, and a slower (30-year) amplifying wind trend eventually leads to eddy heat flux surpassing Ekman transport by a factor of three.

Antarctic sea ice melts in the austral summer, refreezes during winter, and reaches its maximum area in the spring (September–October–November, SON). The seasonal cycle

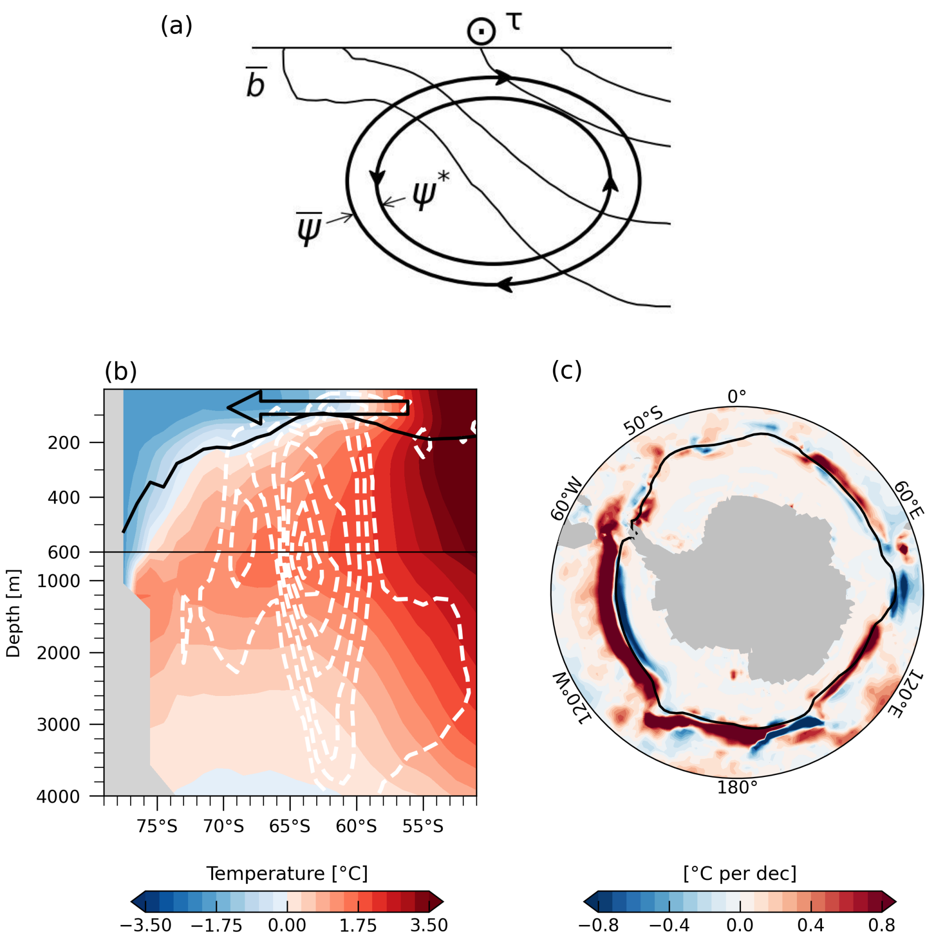

Fig. 2. Eddy-driven MOC (Ψ^*) and poleward heat transport into the seasonal sea ice zone. (a) Schematic of the wind-driven ($\tau, \overline{\Psi}$) and eddy-driven (Ψ^*) components of the Southern Ocean MOC, modified from Marshall & Radko (2003) (57). The sloping lines denote mean buoyancy surfaces. (b) Vertical cross section of the climatological temperature of the ocean (colors; ℃) and the depth of the mixed layer (black curve; m) during spring, along with anomalies driven by eddies Ψ^* (white contours; Sv) during the decadal period of retreat of sea ice, from piControl. Dashed white contours represent eddy-driven Ψ^* anomalies ranging from -0.975 to -0.1 Sv with an interval of 0.125 Sv. The vertical axis for depth ≤ 600 m is expanded for visualization. The black arrow indicates the eddy-driven v^*. (c) Upper-ocean eddy-driven meridional heat flux convergence (averaged above 100 m) during the decadal period of sea ice retreat from piControl (colors; ℃ per decade). The black contour denotes the climatological Antarctic sea-ice edge during spring.

of Antarctic SIE and sea ice concentration (SIC) is captured in a fully coupled climate model, denoted GISS-E2.1-G (Materials and Methods and SI Appendix, Fig. S1). Using a 300-year preindustrial control simulation (denoted as "piControl") from this model, we will investigate to what extent internal variability can explain the observed decadal fluctuations in Antarctic SIE. The rate of change in upper ocean temperature is driven by the synoptic variability of the SAM and the low-frequency mesoscale ocean processes that are parameterized. To further illustrate our hypothesis that stochastic forcing by the wind results in decadal variability of the eddy-driven MOC and associated heat transport, we also present a first-order autoregressive model (AR(1)) (63, 64) in which wind forcing is represented as white noise and ocean eddies as a damping process. To begin, we examine the decadal trends of Antarctic SIE in observations and piControl.

Decadal trends of Antarctic SIE

The observed decadal trends of Antarctic SIE, characterized by a gradual three-decade increase followed by a sharp decadal decline, remain consistent across all four seasons (SI Appendix, Fig. S2). To evaluate changes in maximum SIE, we focus primarily on the spring season. The decadal trending periods are then identified based on the maximum and minimum values, while ensuring they remain non-overlapping. The maximum decadal advance trend observed in the spring SIE is approximately $+0.60 \times 10^6$ km^2 per decade during 2000–2010, while the minimum decadal decline trend is approximately -1.65×10^6 km^2 per decade during 2013–2023 (Fig. 1a).

To examine whether the observed decadal SIE trends can be distinguished from unforced, naturally occurring trends, we compare the magnitude of observed decadal trends with those of piControl, following Polvani and Smith (2013) (35). In piControl, which excludes anthropogenic external forcings, decadal-scale trends in Antarctic SIE—both increasing and decreasing—are present with magnitudes comparable to the observed trends (picked out by the colored bands in Fig. 3a). Figure 1b shows the probability density distribution of 11-year SIE trends derived from piControl. Specifically, we calculate all consecutive, overlapping decadal trends from the initial year onward using the 300-year time series (Materials and Methods). It is worth noting that neither the observed maximum nor minimum 11-year trends differ significantly from the naturally occurring ones. We also examine the probability density distributions for 15-year, 21-year, and 25-year trends, which similarly reveal that there is no significant deviation of the observed extremes from natural variability (not shown). In addition, the observed 11-year trend exhibits the most distinct negative decadal trend among all cases.

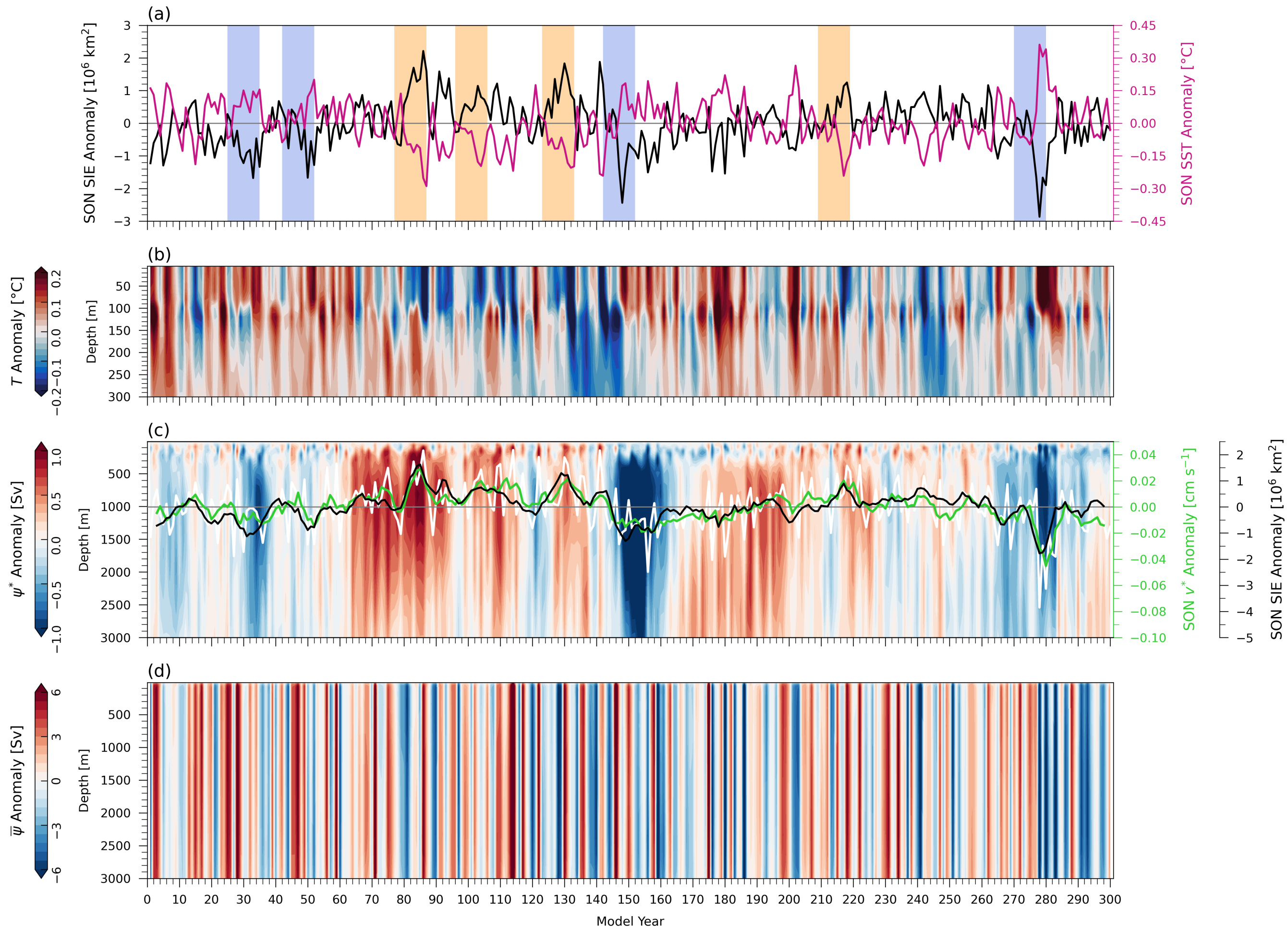

Fig. 3. High-frequency versus low-frequency variabilities across the Southern Ocean in piControl. (a) Time series of anomalous spring (SON) Antarctic SIE (black line; 10^6 km^2) and SST (red-violet line). The decadal periods of sea ice advance and retreat are denoted by orange and blue shadings, respectively. The decadal trending periods are identified based on the maximum and minimum values, while ensuring they remain non-overlapping. Hovmöller diagrams of anomalous (b) upper-ocean temperature (colors; ℃), (c) eddy-driven Ψ^* (colors; Sv) and v^* averaged above 100 m (white line; cm s^{-1}), (d) wind-driven $\overline{\Psi}$ (colors; Sv). In (c), 5-year moving average of v^* (green line; cm s^{-1}) and SIE (black line; 10^6 km^2) are also overlaid. All variables, except for SIE, are averaged between 57.5°S and 67.5°S, and all variables are simulated from piControl.

We then performed composite analyses to examine the spatial distribution of decadal changes across the Southern Ocean. The difference composite, calculated as half the difference between the positive and negative composites, is shown here with the same sign as the positive composite representing the phase of decadal sea ice advance (Materials and Methods). For example, during the decadal periods of sea ice advance, the observed pattern of spring SIC trend shows the largest positive anomalies along the climatological sea-ice edge (Fig. 1c). Meanwhile, the trend of spring sea surface temperature (SST) shows the strongest cooling anomalies along the same sea-ice edge (Fig. 1d), which is consistent with the advance of the sea ice. These decadal trending patterns of SIC and SST are also well captured in piControl, as shown in Figs. 1 (e and f). In particular, the modeled decadal trend patterns exhibit greater zonal symmetry than the observations (SI appendix, Fig. S3). This is perhaps in part because the composite of simulated trends combines more decadal periods over 300 years, and so somewhat averages out the signal.

Mesoscale ocean heat transport into the seasonal zone of sea ice

The broad stratification of the Southern Ocean is maintained by the interplay of wind, air-sea buoyancy fluxes, and the ocean's residual MOC, which is shown schematically in Fig. 2a. In the framework of residual mean theory (see Marshall and Radko (2003) (57)), the residual MOC (Ψ_{res}) is the sum of the Eulerian mean wind-driven MOC ($\overline{\Psi}$) and the eddy-driven MOC (Ψ^*): $\Psi_{\mathrm{res}} = \overline{\Psi} + \Psi^*$. The zonal wind tends to tilt up buoyancy surfaces and mesoscale eddies tend to flatten them out. In the time mean, the two tend to compensate for one another, hence the name residual. But the timescales of $\overline{\Psi}$ and Ψ^* are very different, the first fast, the second slow. $\overline{\Psi}$ responds almost instantaneously to wind changes (owing to Ekman processes) and "flutters" positive and negative on synoptic timescales (see Fig. 2d). Ψ^*, in contrast, is associated with the return to equilibrium of the tilted buoyancy surface on much longer timescales associated with mesoscale transfer processes (see Fig. 2c and Materials and Methods). These fluctuating overturning cells act on mean temperature gradients and result in fluctuating ocean

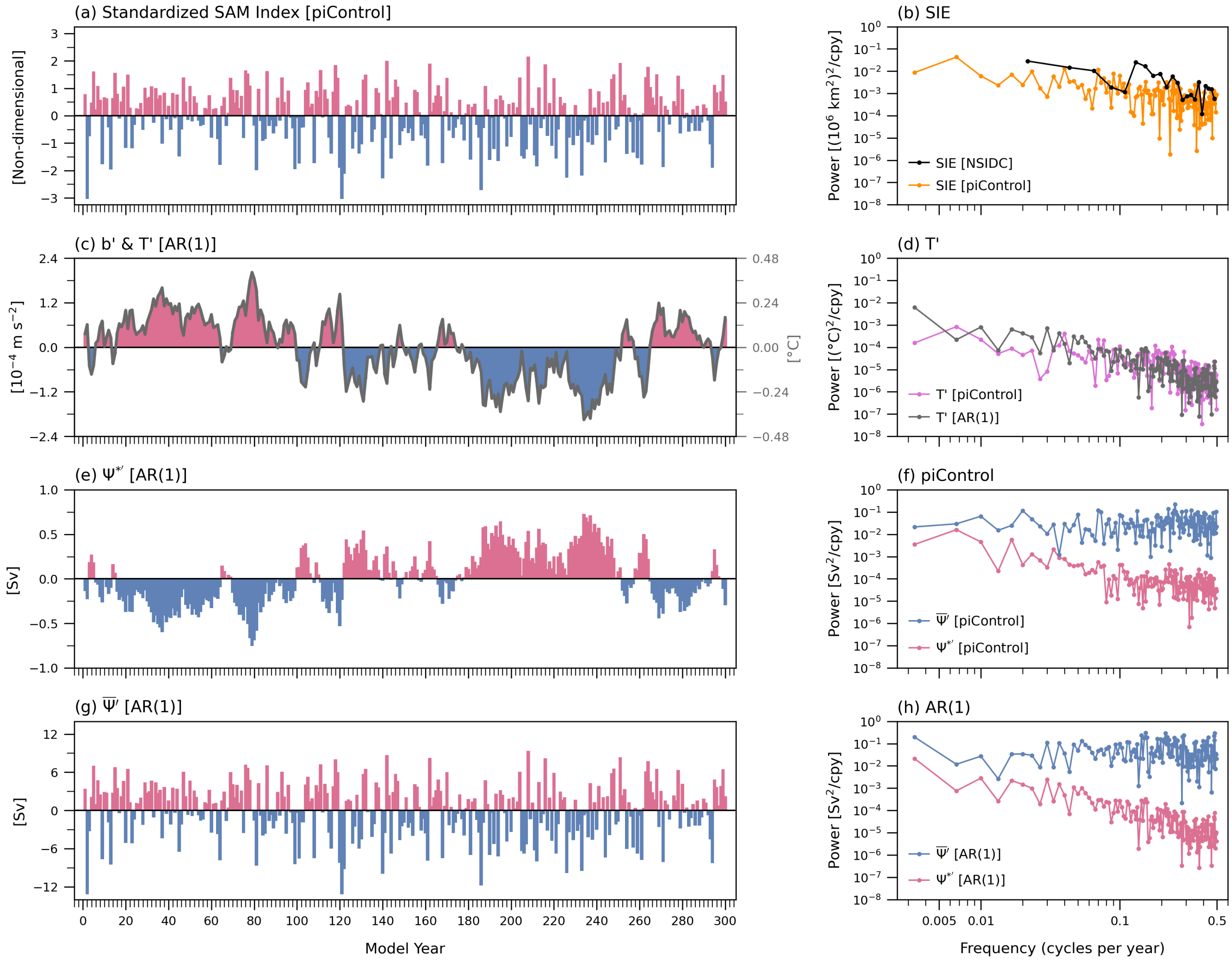

Fig. 4. Southern Ocean's memory as inferred from an idealized stochastic model. (a) Time series of the standardized SAM index from piControl applied to the AR(1) model (bars). Time series of anomalous (c) upper-ocean buoyancy (b'; bars; 10^{-4} m s^{-2}) and temperature (T'; grey line; ℃), (e) eddy-driven $\Psi^{*\prime}$ (bars; Sv), and (g) wind-driven $\overline{\Psi}'$ (bars; Sv) from the AR(1) model. Log-log plot of the power spectrum of anomalous (b) Antarctic SIE ((10^6 km^2)^2/cpy) from NSIDC (black) and piControl (orange), (d) upper-ocean temperature averaged above 100 m (T'; (℃)^2/cpy) from piControl (purple) and the AR(1) model (grey), and wind-driven $\overline{\Psi}'$ (blue; Sv^2/cpy) and eddy-driven Ψ^* (pink; Sv^2/cpy) averaged above 1500 m from (f) piControl and (h) the AR(1) model. All Southern Ocean variables from piControl are averaged between 57.5℃S and 67.5℃S.

heat transports on different timescales. affecting the position of the ice edge.

The upper ocean temperature in the seasonal sea ice zone has a strong meridional gradient across it: approximately between 57.5°S and 67.5°S (Fig. 2b). On decadal timescales, its heat budget includes ocean heat transport, air-sea fluxes, and dissipation terms (Eq. 1; Materials and Methods). During decadal periods of sea ice retreat, diagnostics of our coupled model show that the anomaly in the eddy-driven Ψ^* has an anticlockwise rotation and extends vertically from the surface to depth (see Fig. 2b). Associated with this eddy-driven Ψ^*, the meridional velocity (v^*) is directed southward in the uppermost regions of the ocean (see Eq. 2; Materials and Methods). This southward transport results in a heat flux convergence along the climatological edge of sea ice and the meltback of sea ice during spring (Fig. 2c). In contrast, during the decadal periods of sea ice expansion, the eddy-driven Ψ^* is clockwise (SI Appendix, Fig. S5), leading to northward transport of relatively cold waters and heat flux divergence along the sea-ice edge (SI Appendix, Fig. S6). This ocean heat flux divergence by mesoscale eddies is of a magnitude comparable to the SST cooling trend along the sea-ice edge (see Fig. 1f and SI Appendix, Fig. S6a which have comparable magnitudes) and is therefore a major contributor to the decadal variability of upper ocean temperature and Antarctic SIE.

Stochastic model of Southern Ocean decadal variability driven by winds and damped by the mesoscale

Figure 3a presents the 300-year time series of anomalous spring Antarctic SIE and Southern Ocean SST from piControl. The SIE and SST exhibit a strong inverse correlation and display high- and low-frequency variabilities. Based on the dynamics discussed previously of the Southern Ocean MOC, these two distinct time-scale variabilities could be modulated by the wind-driven $\overline{\Psi}$ and eddy-driven Ψ^* circulations, respectively. For example, the wind-driven $\overline{\Psi}$ varies on high-frequency timescales (Fig. 3d), forced by atmospheric winds associated with the model SAM, which has a rather white spectrum. In contrast, eddy-driven Ψ^* and associated v^* vary on decadal timescales (Fig. 3c). In particular, the anomalous eddy-driven Ψ^* becomes increasingly prominent during the decadal periods of sea ice advance (when it is positive) and retreat (when it is negative) (Fig. 3a). As shown in Figs. 3a-c, during decades of negative (positive) eddy-driven Ψ^* and v^*, anomalous upper-ocean warming (cooling) occurs, corresponding to the low-frequency sea ice retreat (advance).

To reveal the mechanisms driving the two time-scale variations in properties across the Southern Ocean, we develop an illustrative idealized AR(1) model which draws together three key elements of our proposed mechanism: (i) white-noise atmospheric wind forcing over the ACC orchestrated by the SAM (see Eq. 5 and Fig. 4a); (ii) the wind-driven and eddy-driven components of the Southern Ocean's residual MOC, $\Psi_{\text{res}} = \overline{\Psi} + \Psi^*$ (see Eq. 4); and (iii) the resulting low-frequency anomalies in ocean heat/buoyancy transport to the edge of the seasonal sea ice zone (see Eq. 9), which modulates the ocean temperature and sea ice variations. This idealized AR(1) model is presented in Materials and Methods, along with supporting diagnostics from our coupled climate model.

In response to the SAM, wind-driven $\overline{\Psi}$ and eddy-driven Ψ^* show distinct behaviors on high-frequency and low-frequency timescales in our AR(1) model (Figs. 4g and 4e). Wind-driven $\overline{\Psi}$, through associated Ekman currents, perturbs the tilted buoyancy surfaces (b') from their reference position. However, the mesoscale eddy field relaxes b' back to zero, giving rise to low-frequency variations. The ocean relaxation timescale for this eddy adjustment, governed by variations in the eddy-driven Ψ^*, is estimated to be approximately a decade long, ranging from 16.7 to 9.1 years (Materials and Methods). These fluctuations in the MOC induce fluctuations in the transport of meridional eddy buoyancy (and heat) transport (Fig. 4c), which are then imagined to modulate the Antarctic SIE.

We further analyze the power spectrum of key variables, which offers an effective representation of time variability. Antarctic SIE exhibits a "red" spectrum, with elevated low-frequency variability, in both observations and piControl (Fig. 4b). Comparing the model spectra of ocean variables from piControl with the theoretical spectra from the AR(1) model, we find that both have a similar form. For example, the spectrum of upper ocean temperature anomalies shows a red signal. Similarly, for the Southern Ocean MOC, the eddy-driven Ψ^* shows a red spectrum, whereas the wind-driven $\overline{\Psi}$ is white. Relaxation of the mesoscale eddy field damps high-frequency variability to produce a slow response, a "reddening" of the spectrum of climate variability.

Discussion and Conclusions

The ocean exhibits long memory, integrating short-term random noise into longer-term unforced variations, manifested as red spectra. The mechanisms underlying low-frequency variability in the North Atlantic and the North Pacific have been extensively studied over a long period ((49–51, 65), and references therein). This study investigates low-frequency variations in the MOC across the Southern Ocean modulated by circulation dynamics on the mesoscale.

Our results show how variations within the seasonal sea ice zone of the Southern Ocean occur at two distinct frequencies. High-frequency variations are the instantaneous response to white noise atmospheric wind forcing through the associated wind-driven wind $\overline{\Psi}$. In contrast, low-frequency variations are modulated by meridional heat transport through associated eddy-driven Ψ^*, reflecting the timescale of ocean relaxation over decades due to geostrophic eddies. The slow eddy adjustment drives decadal warming and cooling of the upper ocean temperature and associated waxing and waning of the sea ice edge.

Such processes could have contributed to a decrease in SIE comparable to that observed in the past decade. This may suggest that the recent dramatic retreat of Antarctic sea ice could be a manifestation of natural climate variability rather than of anthropogenic origin. Future work should explore how these natural oscillations interact with externally forced changes, such as surface warming, freshening and wind variations, all of which might affect ocean eddy processes. Such efforts could be addressed through diagnoses of historical simulations and future projections across various climate scenarios, and diagnosis of models that resolve, rather than parameterize, the all-important mesoscale.

Materials and Methods

Observations. Here we use the monthly Antarctic SIE index during 1979–2024 obtained from the National Snow and Ice Data Center (NSIDC) Version 3 (66). The monthly Antarctic SIC during 1979–2024 is obtained from the Copernicus Climate Change Service (C3S) (67). The SIE is defined as the ocean surface area that contains sea ice exceeding the threshold value of 15%. The SST dataset during 1979–2024 is obtained from ECMWF Reanalysis v5 (ERA5) (68).

The coupled climate model. We employ the E2.1-G version of the National Aeronautics and Space Administration (NASA) Goddard Institute for Space Studies (GISS) Earth system model, denoted GISS-E2.1-G (69–71). GISS-E2.1-G is a coupled climate model designed to simulate the earth system comprising representations of the atmosphere, ocean, land and sea ice (SI Appendix). The GISS-E2.1-G model has a substantially improved climatology in a long piControl simulation, particularly in its representation of the Southern Hemisphere atmosphere, ocean and sea-ice distributions — see Kelley *et al.* (2020) (69) and Miller *et al.* (2021) (70). The model simulates a notably realistic mixed layer depth distribution in the Southern Ocean, suggesting that convection forms in plausible locations along the Antarctic continental shelf. The modeled seasonal cycle of Antarctic sea ice also agrees rather well with observations (69).

Probability Density Distributions (pdfs) of decadal trends in Antarctic SIE.. Following Polvani & Smith (2013) (35), we calculate all consecutive, overlapping decadal trends from the initial year onward using the 300-year time series shown in Fig. 3a. The probability density distributions are then computed from these decadal trends using a kernel density estimator, providing a nonparametric, smoothed fit to the data. Each curve has an area of one. We also present the count for each range of decadal trends in Fig. 1b.

For example, we calculate the exact probability density distribution of 27-year decadal trends in Antarctic SIE, obtaining distributions similar to those of Polvani & Smith (2013) (35), as shown in SI Appendix, Fig. S4. We further calculate the probability density distribution of 11-year decadal trends, highlighting the recent decadal decline, as shown in Fig. 1b. We also calculate the probability density distributions for 15-year, 21-year, and 25-year trends, finding that neither the observed maximum nor minimum decadal trends differ significantly from naturally occurring ones. The observed 11-year decadal trend exhibits the most distinct negative trend among them.

Composite analyses. In our diagnostic analysis, we define the phases of sea ice advance and retreat as those characterized by upward and downward decadal trends in Antarctic SIE, respectively, as identified in Fig. 1a for the observations (i.e., NSIDC, ERA5) and in Fig. 3a for the piControl of GISS-E2.1-G. We first compute composites for the upward decadal trends and separately for the downward decadal trends. Each composite is based on one member for the observations and four members for the piControl. The difference composite is then computed as half the magnitude of the difference between the two composites. An example of the resulting difference composite is shown in Figs. 1 (c-f).

The upper-ocean (e.g. 100m) temperature perturbation (T') appropriate for trend periods can be written as follows:

$$\frac{\partial \langle T' \rangle}{\partial t} = -v^{*'} \cdot \widetilde{T_y} + \cdots, \qquad [1]$$

where T' is the upper ocean temperature anomaly, T_y is the meridional gradient of ocean temperature, $v^{*'}$ is the eddy-driven meridional velocity anomaly and $(\cdots)$ represent all other terms. The tilde $(\widetilde{\ })$ denotes a time average, the prime $(')$ denotes the anomaly from that time average, and the angle bracket $\langle\ \rangle$ denotes a vertical average over the upper 100 m of ocean. The $v^{*'}$ can be written as:

$$v^{*'} = -\Psi^{*'}_z, \qquad [2]$$

where $\Psi^{*'}$ is the eddy-driven MOC anomaly. The $()_y$ and $()_z$ denote meridional and vertical gradients, respectively.

The contribution of eddy-driven advection to upper ocean decadal trends shown in Fig. 2c, for example, is obtained by compositing the term over those decadal periods. All other terms contributing to the tendency can be presented in the same way.

An idealized stochastic model. Following the framework of zonal-average residual mean theory (57), we write the dominant terms in the subsurface buoyancy equation thus:

$$\frac{\partial b'}{\partial t} + v'_{\mathrm{res}} \cdot \widetilde{b_y} = 0, \qquad [3]$$

where b' is the ocean buoyancy anomaly, $\widetilde{b_y}$ is the mean meridional gradient of ocean buoyancy, and the tilde $(\widetilde{\ })$ denotes a time average. Here $v'_{\mathrm{res}} = \overline{v}' + v^{*'}$ is the meridional residual velocity anomaly comprising wind and eddy-driven components

$$\begin{cases} \overline{v}' = -\overline{\Psi}'_z = -\dfrac{1}{H}\left(-\dfrac{\tau'}{\rho_0 f}\right) \\ v^{*'} = -\Psi^{*'}_z = -\dfrac{1}{H}\left(-K\dfrac{b'_y}{\widetilde{b_z}}\right) \end{cases}, \qquad [4]$$

where H is the depth of the diabatic mesoscale layer, K is the mesoscale eddy transfer coefficient, ρ_0 is a constant ocean density, f is the Coriolis parameter, $\widetilde{b_z}$ is the mean stratification and τ' is the atmospheric zonal wind stress anomaly over the ACC. Below, b'_y is replaced as b'/L, where L is the meridional scale of eddy-driven $\Psi^{*'}$ to obtain a tractable mathematical form that can easily be solved.

Expressing the wind forcing as:

$$\tau' = \tau_0 \cdot W(t), \qquad [5]$$

where τ_0 is an amplitude and $W(t)$ is a white noise process, and summing the two contributions to v'_{res}, we obtain:

$$v'_{\mathrm{res}} = \frac{\tau_0}{\rho_0 f H} W(t) + \frac{K}{HL}\frac{b'}{\widetilde{b_z}}. \qquad [6]$$

The first term represents the action of the wind and covaries with it, the second represents the effect of mesoscale eddies returning tilted density surfaces to equilibrium on a timescale set by the mesoscale eddy diffusivity and the slope of mean buoyancy surfaces.

Substituting Eq. 6 into Eq. 3 and for the wind-forcing assumed in Eq. 5, we arrive at an AR(1) model driven by white noise wind forcing and reddened by the ocean's mesoscale:

$$\frac{\partial \mathbb{B}}{\partial t} + \underbrace{\frac{1}{\tau_{\mathrm{relax}}}\mathbb{B}}_{\text{Ocean relaxation}} = \underbrace{-W(t)}_{\text{White noise}}. \qquad [7]$$

where

$$\mathbb{B} = \frac{b'}{\frac{\tau_0 \widetilde{b_y}}{\rho_0 f H}}, \qquad [8]$$

is a scaled buoyancy and

$$\tau_{\mathrm{relax}} = -\frac{HL}{K s_\rho}, \qquad [9]$$

is a relaxation timescale set by mesoscale eddies where $s_\rho = -\widetilde{b_y}/\widetilde{b_z}$ is the slope of mean buoyancy surfaces.

Numbers. Our choice of parameters for the AR(1) model is guided through diagnoses of the coupled model. They are shown in Extended Data Table S1. Estimates of K and τ_0 are obtained from zonal-mean values in the mid-latitude Southern Ocean between 57.5°S to 67.5°S. We plotted $v^{*'}$ and found it to be primarily confined to the upper 100 m, giving us an estimate of H. L is approximately 10° latitude, representing the meridional scale of eddy-driven $\Psi^{*'}$. s_ρ is the slope of mean buoyancy surfaces, ranging from 2.1×10^{-4} through 3.0×10^{-4} to 3.3×10^{-4}, as shown in SI Appendix, Fig. S7. The implied relaxation timescale, Eq. 9, is then estimated to range from 16.7 through 11.1 to 9.1 years i,e, is roughly decadal.

We can estimate b' from $g \cdot \alpha_T \cdot T'$, where g is the acceleration of gravity, α_T is a thermal expansion coefficient typical of the cold surface around Antarctica, and T' is the estimated numerical upper ocean temperature perturbation, as shown in Fig. 4c.

Data, Materials, and Software Availability. All study data are included in the article and / or the SI Appendix. The data sets analyzed in this study are all publicly available. The GISS-E2.1-G model components are open source and available at https://data.giss.nasa.gov/modelE/cmip6/. The piControl of GISS-E2.1-G output will be stored on the NCCS public data portal (e.g., https://portal.nccs.nasa.gov/datashare/). All data sets and Python scripts used for the analyses described in this study will be made available in a GitHub repository.

ACKNOWLEDGMENTS. Q.L. and J.M. are supported by the NASA MAP program 19-MAP19-0011 and the MIT-GISS cooperative agreement. Model simulations and analysis were performed on the NASA High End Computing (HEC) Program through the NASA Center for Climate Simulation (NCCS) at the Goddard Space Flight Center.

1. A Riihelä, RM Bright, K Anttila, Recent strengthening of snow and ice albedo feedback driven by Antarctic sea-ice loss. *Nat. Geosci.* **14**, 832–836 (2021).
2. CJ Wall, T Kohyama, DL Hartmann, Low-cloud, boundary layer, and sea ice interactions over the Southern Ocean during winter. *J. Clim.* **30**, 4857–4871 (2017).
3. X Yuan, DG Martinson, Antarctic sea ice extent variability and its global connectivity. *J. Clim.* **13**, 1697–1717 (2000).
4. KI Ohshima, et al., Antarctic Bottom Water production by intense sea-ice formation in the Cape Darnley polynya. *Nat. Geosci.* **6**, 235–240 (2013).
5. RP Abernathey, et al., Water-mass transformation by sea ice in the upper branch of the southern ocean overturning. *Nat. Geosci.* **9**, 596–601 (2016).
6. R Ferrari, et al., Antarctic sea ice control on ocean circulation in present and glacial climates. *Proc. Natl. Acad. Sci.* **111**, 8753–8758 (2014).
7. BB Stephens, RF Keeling, The influence of Antarctic sea ice on glacial–interglacial CO_2 variations. *Nature* **404**, 171–174 (2000).
8. B Delille, et al., Southern Ocean CO_2 sink: The contribution of the sea ice. *J. Geophys. Res. Ocean.* **119**, 6340–6355 (2014).
9. H Eicken, The role of sea ice in structuring Antarctic ecosystems. *Polar Biol.* **12**, 3–13 (1992).
10. KM Swadling, et al., Biological responses to change in Antarctic sea ice habitats. *Front. Ecol. Evol.* **10** (2023).

11. RA Massom, et al., Antarctic ice shelf disintegration triggered by sea ice loss and ocean swell. *Nature* **558**, 383–389 (2018).
12. D Notz, J Stroeve, Observed Arctic sea-ice loss directly follows anthropogenic CO_2 emission. *Science* **354**, 747–750 (2016).
13. J Stroeve, D Notz, Changing state of arctic sea ice across all seasons. *Environ. Res. Lett.* **13**, 103001 (2018).
14. R Chemke, LM Polvani, JE Kay, C Orbe, Quantifying the role of ocean coupling in Arctic amplification and sea-ice loss over the 21st century. *npj Clim. Atmospheric Sci.* **4**, 46 (2021).
15. T Fan, C Deser, DP Schneider, Recent Antarctic sea ice trends in the context of Southern Ocean surface climate variations since 1950. *Geophys. Res. Lett.* **41**, 2419–2426 (2014).
16. FA Haumann, D Notz, H Schmidt, Anthropogenic influence on recent circulation-driven Antarctic sea ice changes. *Geophys. Res. Lett.* **41**, 8429–8437 (2014).
17. A Purich, W Cai, MH England, T Cowan, Evidence for link between modelled trends in Antarctic sea ice and underestimated westerly wind changes. *Nat. Commun.* **7**, 10409 (2016).
18. CL Parkinson, A 40-y record reveals gradual Antarctic sea ice increases followed by decreases at rates far exceeding the rates seen in the Arctic. *Proc. Natl. Acad. Sci.* **116**, 14414–14423 (2019).
19. J Turner, et al., Unprecedented springtime retreat of Antarctic sea ice in 2016. *Geophys. Res. Lett.* **44**, 6868–6875 (2017).
20. GA Meehl, et al., Sustained ocean changes contributed to sudden Antarctic sea ice retreat in late 2016. *Nat. Commun.* **10**, 14 (2019).
21. G Wang, et al., Compounding tropical and stratospheric forcing of the record low Antarctic sea-ice in 2016. *Nat. Commun.* **10**, 13 (2019).
22. E Gilbert, C Holmes, 2023's Antarctic sea ice extent is the lowest on record. *Weather* **79**, 46–51 (2024).
23. M Ionita, Large-scale drivers of the exceptionally low winter Antarctic sea ice extent in 2023. *Front. Earth Sci.* **2** (2024).
24. C Eayrs, X Li, MN Raphael, DM Holland, Rapid decline in Antarctic sea ice in recent years hints at future change. *Nat. Geosci.* **14**, 460–464 (2021).
25. RL Fogt, AM Sleinkofer, MN Raphael, MS Handcock, A regime shift in seasonal total Antarctic sea ice extent in the twentieth century. *Nat. Clim. Chang.* **12**, 54–62 (2022).
26. A Purich, EW Doddridge, Record low Antarctic sea ice coverage indicates a new sea ice state. *Commun. Earth & Environ.* **4**, 314 (2023).
27. W Hobbs, et al., Observational evidence for a regime shift in summer Antarctic sea ice. *J. Clim.* **37**, 2263–2275 (2024).
28. S Solomon, GK Plattner, R Knutti, P Friedlingstein, Irreversible climate change due to carbon dioxide emissions. *Proc. Natl. Acad. Sci.* **106**, 1704–1709 (2009).
29. DWJ Thompson, S Solomon, Interpretation of recent southern hemisphere climate change. *Science* **296**, 895–899 (2002).
30. MC Serreze, WN Meier, The arctic's sea ice cover: trends, variability, predictability, and comparisons to the Antarctic. *Annals New York Acad. Sci.* **1436**, 36–53 (2019).
31. J Turner, JS Hosking, TJ Bracegirdle, GJ Marshall, T Phillips, Recent changes in antarctic sea ice. *Philos. Transactions Royal Soc. A: Math. Phys. Eng. Sci.* **373**, 20140163 (2015).
32. WR Hobbs, et al., A review of recent changes in Southern Ocean sea ice, their drivers and forcings. *Glob. Planet. Chang.* **143**, 228–250 (2016).
33. T Maksym, Arctic and antarctic sea ice change: Contrasts, commonalities, and causes. *Annu. Rev. Mar. Sci.* **11**, 187–213 (2019).
34. V Zunz, H Goosse, F Massonnet, How does internal variability influence the ability of CMIP5 models to reproduce the recent trend in Southern Ocean sea ice extent? *The Cryosphere* **7**, 451–468 (2013).
35. LM Polvani, KL Smith, Can natural variability explain observed Antarctic sea ice trends? New modeling evidence from CMIP5. *Geophys. Res. Lett.* **40**, 3195–3199 (2013).
36. MÈ Gagné, NP Gillett, JC Fyfe, Observed and simulated changes in Antarctic sea ice extent over the past 50 years. *Geophys. Res. Lett.* **42**, 90–95 (2015).
37. H Goosse, V Zunz, Decadal trends in the Antarctic sea ice extent ultimately controlled by ice–ocean feedback. *The Cryosphere* **8**, 453–470 (2014).
38. SE Stammerjohn, DG Martinson, RC Smith, X Yuan, D Rind, Trends in Antarctic annual sea ice retreat and advance and their relation to El Niño–Southern Oscillation and Southern Annular Mode variability. *J. Geophys. Res. Ocean.* **113** (2008).
39. A Purich, et al., Tropical pacific SST drivers of recent Antarctic sea ice trends. *J. Clim.* **29**, 8931–8948 (2016).
40. GA Meehl, JM Arblaster, CM Bitz, CTY Chung, H Teng, Antarctic sea-ice expansion between 2000 and 2014 driven by tropical pacific decadal climate variability. *Nat. Geosci.* **9**, 590–595 (2016).
41. X Crosta, et al., Multi-decadal trends in Antarctic sea-ice extent driven by ENSO–SAM over the last 2,000 years. *Nat. Geosci.* **14**, 156–160 (2021).
42. Y Liu, et al., Decadal oscillation provides skillful multiyear predictions of Antarctic sea ice. *Nat. Commun.* **14**, 8286 (2023).
43. DB Bonan, J Dörr, RCJ Wills, AF Thompson, M Årthun, Sources of low-frequency variability in observed Antarctic sea ice. *The Cryosphere* **18**, 2141–2159 (2024).
44. L Zhang, TL Delworth, W Cooke, X Yang, Natural variability of Southern Ocean convection as a driver of observed climate trends. *Nat. Clim. Chang.* **9**, 59–65 (2019).
45. L Zhang, et al., The relative role of the subsurface Southern Ocean in driving negative Antarctic sea ice extent anomalies in 2016–2021. *Commun. Earth & Environ.* **3**, 302 (2022).
46. S Rathore, NL Bindoff, HE Phillips, M Feng, Recent hemispheric asymmetry in global ocean warming induced by climate change and internal variability. *Nat. Commun.* **11**, 2008 (2020).
47. KC Armour, J Marshall, JR Scott, A Donohoe, ER Newsom, Southern Ocean warming delayed by circumpolar upwelling and equatorward transport. *Nat. Geosci.* **9**, 549–554 (2016).
48. J Marshall, RA Plumb, *Atmosphere, Ocean, and Climate Dynamics: An Introductory Text*, International Geophysics Series, vol. 93. (Elsevier Academic Press), 1st edition, pp. 259–265 (2008).
49. DV Hansen, HF Bezdek, On the nature of decadal anomalies in North Atlantic sea surface temperature. *J. Geophys. Res. Ocean.* **101**, 8749–8758 (1996).
50. J Namias, RM Born, Temporal coherence in North Pacific sea-surface temperature patterns. *J. Geophys. Res. (1896-1977)* **75**, 5952–5955 (1970).
51. C Deser, MA Alexander, SP Xie, AS Phillips, Sea surface temperature variability: Patterns and mechanisms. *Annu. Rev. Mar. Sci.* **2**, 115–143 (2010).
52. JR Toggweiler, J Russell, Ocean circulation in a warming climate. *Nature* **451**, 286–288 (2008).
53. J Marshall, K Speer, Closure of the meridional overturning circulation through Southern Ocean upwelling. *Nat. Geosci.* **5**, 171–180 (2012).
54. D Ferreira, J Marshall, CM Bitz, S Solomon, A Plumb, Antarctic ocean and sea ice response to ozone depletion: A two-time-scale problem. *J. Clim.* **28**, 1206–1226 (2015).
55. Q Li, MH England, AM Hogg, Transient response of the Southern Ocean to idealized wind and thermal forcing across different model resolutions. *J. Clim.* **34**, 5477–5496 (2021).
56. AK Morrison, DW Waugh, AM Hogg, DC Jones, RP Abernathey, Ventilation of the Southern Ocean pycnocline. *Annu. Rev. Mar. Sci.* **14**, 405–430 (2022).
57. J Marshall, T Radko, Residual-mean solutions for the Antarctic Circumpolar Current and its associated overturning circulation. *J. Phys. Oceanogr.* **33**, 2341–2354 (2003).
58. D Olbers, M Visbeck, A model of the zonally averaged stratification and overturning in the Southern Ocean. *J. Phys. Oceanogr.* **35**, 1190–1205 (2005).
59. SP Bishop, et al., Southern Ocean overturning compensation in an eddy-resolving climate simulation. *J. Phys. Oceanogr.* **46**, 1575–1592 (2016).
60. MP Meredith, AM Hogg, Circumpolar response of Southern Ocean eddy activity to a change in the Southern Annular Mode. *Geophys. Res. Lett.* **33** (2006).
61. AM Treguier, J Le Sommer, JM Molines, B de Cuevas, Response of the Southern Ocean to the Southern Annular Mode: Interannual variability and multidecadal trend. *J. Phys. Oceanogr.* **40**, 1659–1668 (2010).
62. AMC Hogg, MP Meredith, JR Blundell, C Wilson, Eddy heat flux in the Southern Ocean: Response to variable wind forcing. *J. Clim.* **21**, 608–620 (2008).
63. K Hasselmann, Stochastic climate models Part I. Theory. *Tellus* **28**, 473–485 (1976).
64. DW Pierce, Distinguishing coupled ocean–atmosphere interactions from background noise in the North Pacific. *Prog. Oceanogr.* **49**, 331–352 (2001).
65. H Khatri, RG Williams, T Woollings, DM Smith, An ocean memory perspective: Disentangling atmospheric control of decadal variability in the North Atlantic Ocean. *Geophys. Res. Lett.* **51**, e2024GL110333 (2024).
66. F Fetterer, K Knowles, WN Meier, M Savoie, AK Windnagel, Sea ice index, version 3 (2017) Available online at https://nsidc.org/data/G02135/versions/3.
67. T Lavergne, et al., Version 2 of the EUMETSAT OSI SAF and ESA CCI sea-ice concentration climate data records. *The Cryosphere* **13**, 49–78 (2019) Available online at https://cds.climate.copernicus.eu/datasets/satellite-sea-ice-concentration?tab=overview.
68. H Hersbach, et al., The ERA5 global reanalysis. *Q. J. Royal Meteorol. Soc.* **146**, 1999–2049 (2020).
69. M Kelley, et al., GISS-E2.1: Configurations and climatology. *J. Adv. Model. Earth Syst.* **12**, e2019MS002025 (2020).
70. RL Miller, et al., CMIP6 historical simulations (1850–2014) with GISS-E2.1. *J. Adv. Model. Earth Syst.* **13**, e2019MS002034 (2021).
71. LS Nazarenko, et al., Future climate change under ssp emission scenarios with giss-e2.1. *J. Adv. Model. Earth Syst.* **In press**, e2021MS002871 (2022).

PNAS

Supporting Information for

Natural Decadal Variability of Antarctic Sea Ice Modulated by Mesoscale Ocean Memory

Qian Li & John Marshall

Corresponding Author: Qian Li
E-mail: qian_li@mit.edu

This PDF file includes:

Supporting text
Figs. S1 to S7
Table S1
SI References

Supporting Information Text

Model configuration of the GISS-E2.1-G

The atmospheric model component has a horizontal resolution of 2°× 2.5° latitude by longitude and 40 vertical pressure layers. The vertical coordinate transitions from a terrain-following sigma tropospheric representation below 150 hPa to constant pressure stratospheric layers above this level, all the way up to the model top at 0.1 hPa. The dynamical core, atmospheric mixing, convection, and boundary layer models are described in more detail in Kelley et al. (2020) (1).

The ocean model component of E2.1-G version has a horizontal resolution of 1°× 1.25° latitude by longitude and 40 vertical layers. It is mass-conserving with free surface and natural surface boundary conditions for heat and freshwater flows (2). The model employs a version of the boundary layer K-profile parameterization (KPP) of vertical mixing (3) and the Gent and McWilliams (GM) parameterization (4) with variable coefficients (5) for eddy tracer fluxes induced by mesoscale baroclinic turbulence. In E2.1-G, the parameterization of mesoscale eddy transport is updated with a moderate complexity 3D mesoscale diffusivity inspired by the studies presented in Marshall *et al.* (2017) (6). Vertical diapycnal diffusivity incorporates a new tidal mixing scheme through a dissipation distribution given by Jayne (2009) (7), which improves the representation of the AMOC. Additional developments include the use of higher-order advection schemes (8), finer upper ocean layering, and more realistic representation of the flow through the straits that affect property distributions in marginal seas (1).

The sea-ice model component consists of two mass layers within each of which are two thermal layers. The salinity and tracer values of the sea ice are calculated on the atmospheric grid in the horizontal layers and the mass layers in the vertical. The dynamics of sea ice is based on a formulation of the standard viscous-plastic rheology (9). Sea-ice thermodynamics includes a “Brine Pocket” parameterization (10) that allows salt to play a more active role in the specific heat and melt rates of sea ice.

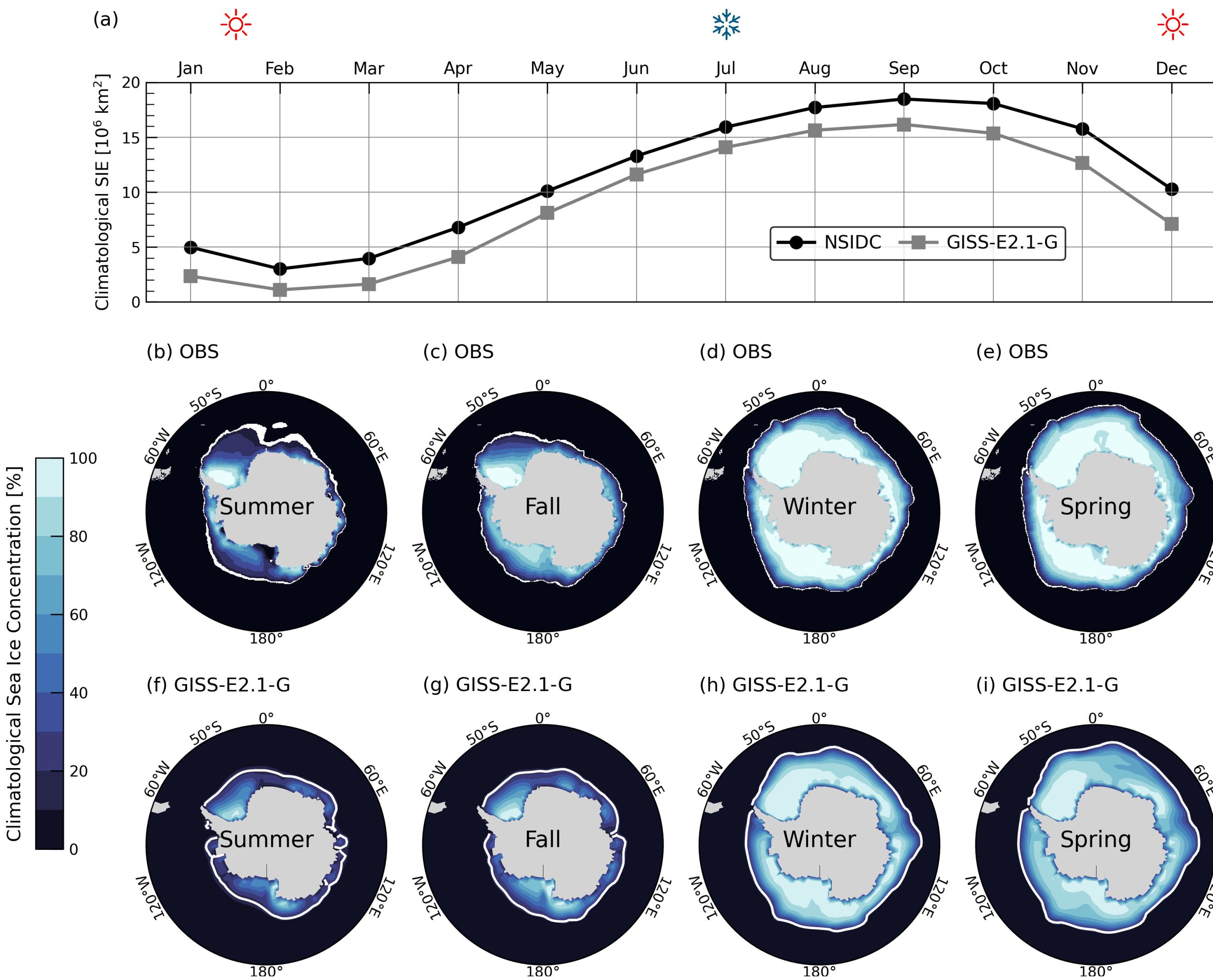

Fig. S1. Climatological Antarctic SIE and SIC. (a) Climatological monthly Antarctic SIE (10^6 km^2) from the NSIDC observation (black line with circular markers) and piControl (grey line with square markers). Climatological Antarctic SIC (color; %) in the austral (b, f) summer (December-January-February, DJF), (c, g) fall (March-April-May, MAM), (d, h) winter (June-July-August, JJA), and (e, i) spring (September–October–November, SON) from the satellite observation and piControl, respectively. The white contour denotes the climatological Antarctic sea ice edge during each season.

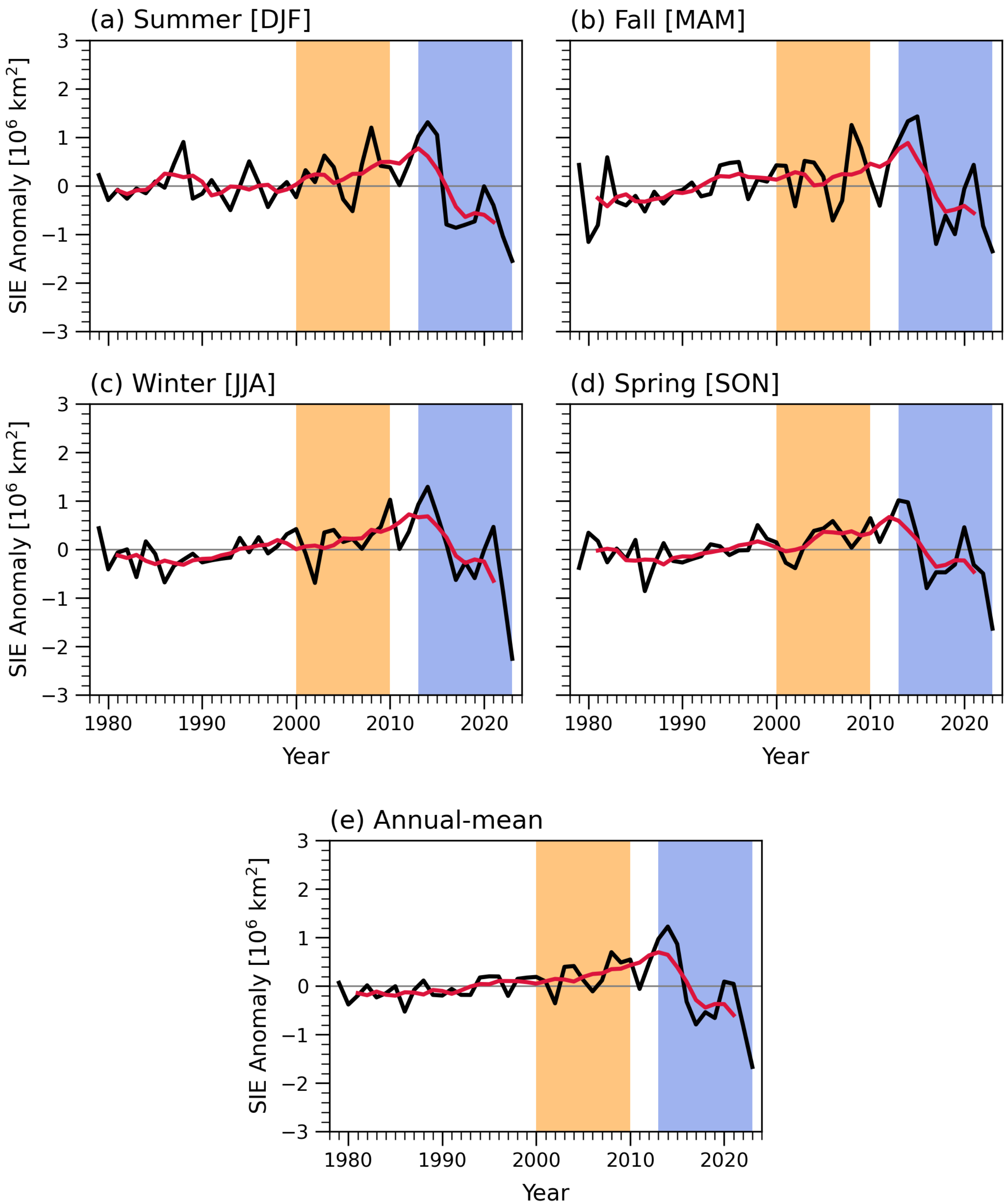

Fig. S2. Observed seasonal time series of Antarctic SIE. Time series of Antarctic SIE anomalies in the austral (a) summer (DJF), (b) fall (MAM), (c) winter (JJA), (d) spring (SON), and (e) annual-mean from the NSIDC observation during 1979–2023. The 5-year moving average (red) is superimposed. The periods of maximum and minimum decadal trends in spring SIE are denoted by the orange and blue shadings, respectively.

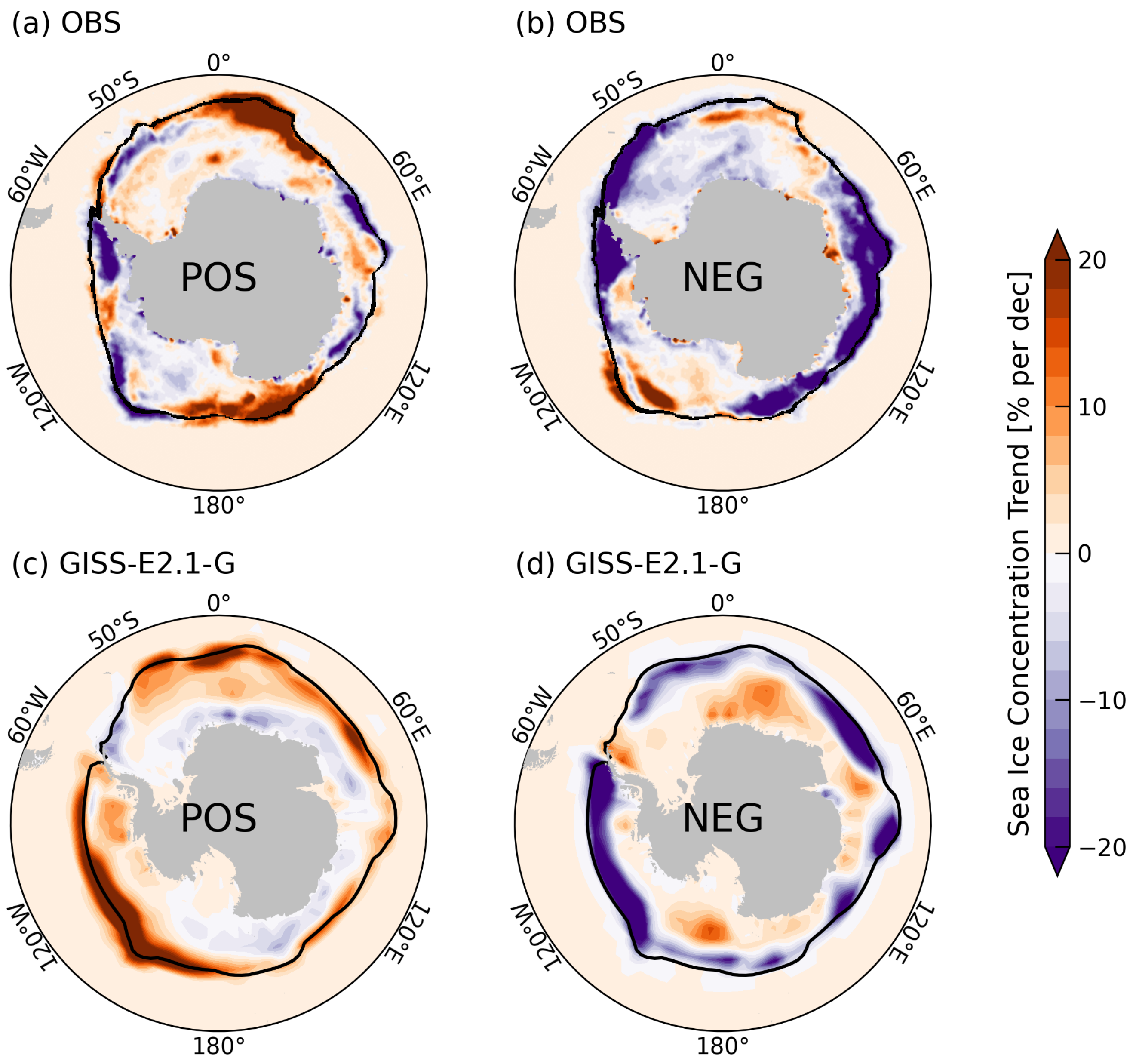

Fig. S3. Spatial distribution of decadal trends in SIC. During the decadal period of sea ice (a, c) advance and (b, d) retreat, 11-year trends in spring Antarctic SIC (color; % per dec) from the satellite observation and piControl, respectively. The Black contour denotes the climatological Antarctic sea ice edge during spring.

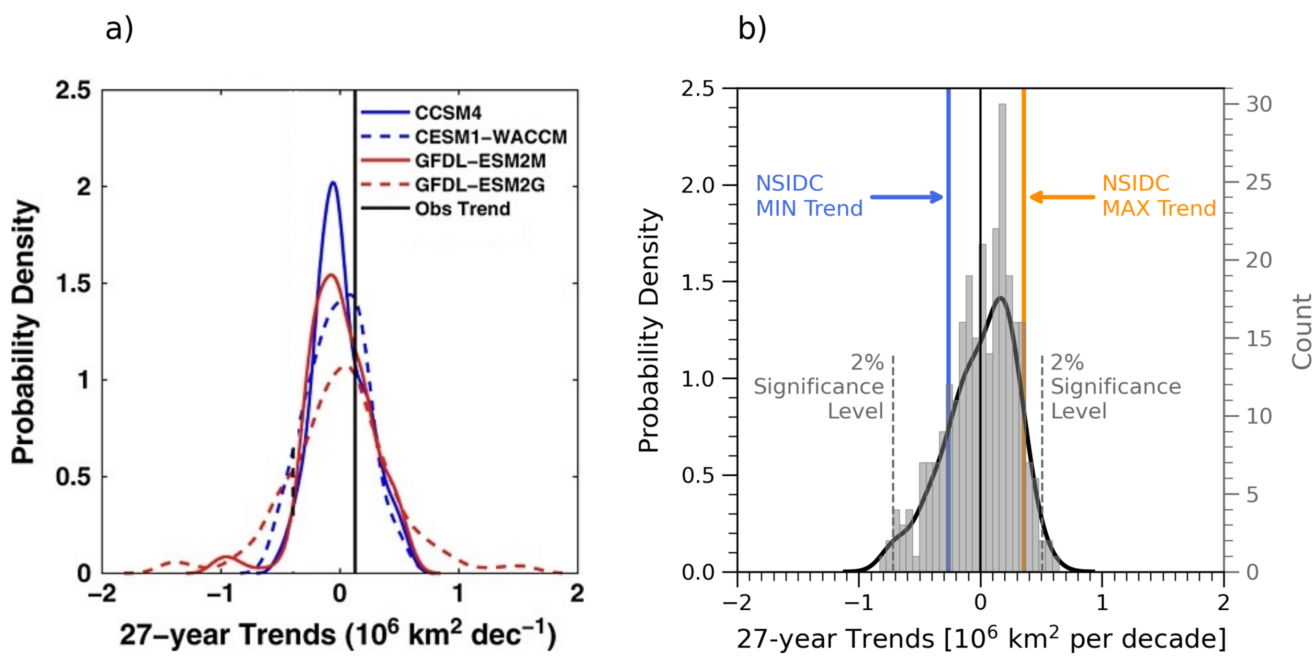

Fig. S4. Decadal trends in Antarctic SIE. Density distributions of 27-year a) four individual climate models, modified from Polvani & Smith (2013)(11), and (b) from GISS-E2.1-G. In a), the observed maximum trend is shown for 1979–2005 (solid black line). In (b), the observed maximum and minimum trends are shown for 1989–2015 (solid orange line) and 1997–2023 (solid blue line), respectively. The dashed grey line indicates the 2% significance level.

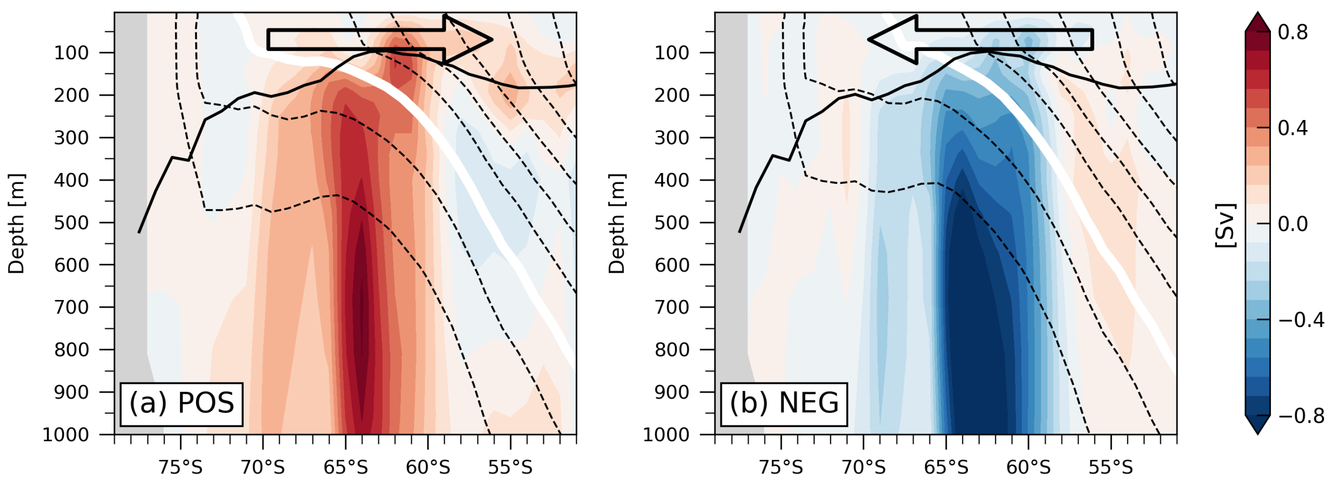

Fig. S5. Eddy-driven MOC. Vertical cross-sections of spring eddy-driven MOC anomalies (color; Sv), potential density (dashed contours; kg m^{-3}), and mixed layer depth (black curve; m) during the decadal period of sea ice (a) advance and (b) retreat, respectively. For the potential density, the value of 27.465 kg m^{-3} is indicated in white, and the contour interval is 0.1 kg m^{-3}. The black arrow indicates the eddy-driven v^{*}.

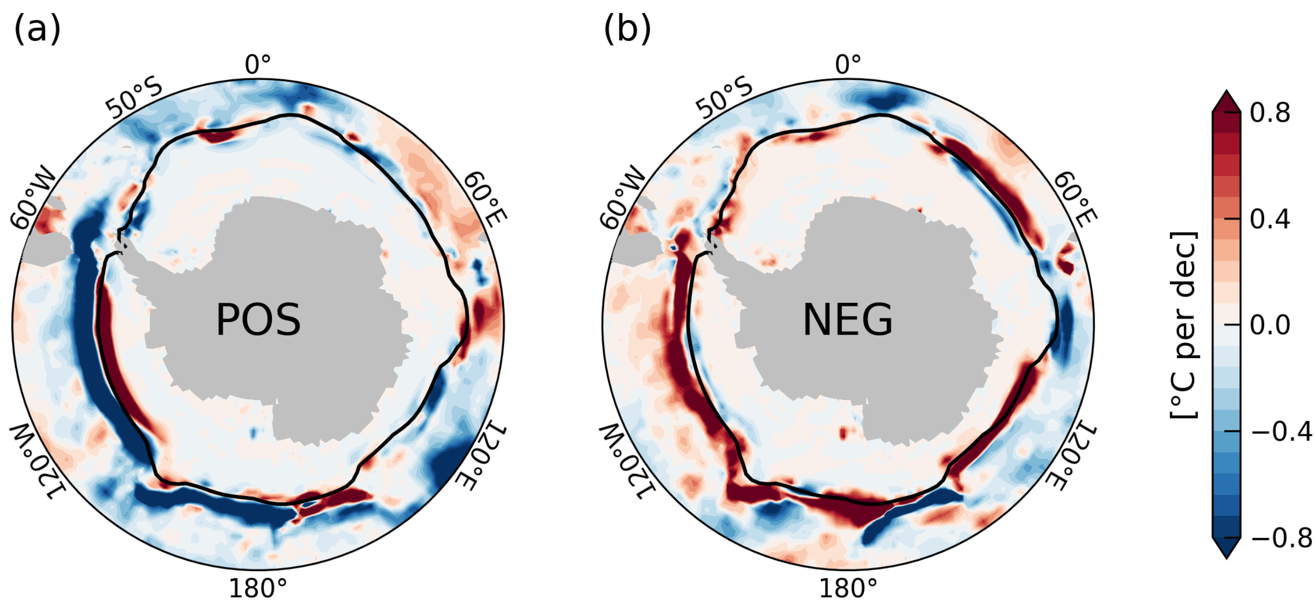

Fig. S6. Eddy-driven meridional heat transport into the seasonal sea ice zone. The upper-ocean (averaged above 100 m) eddy-driven meridional heat flux (a) divergence and (b) convergence (color; ℃ per dec) during the decadal period of sea ice advance and retreat, respectively. The Black contour denotes the climatological Antarctic sea ice edge during spring.

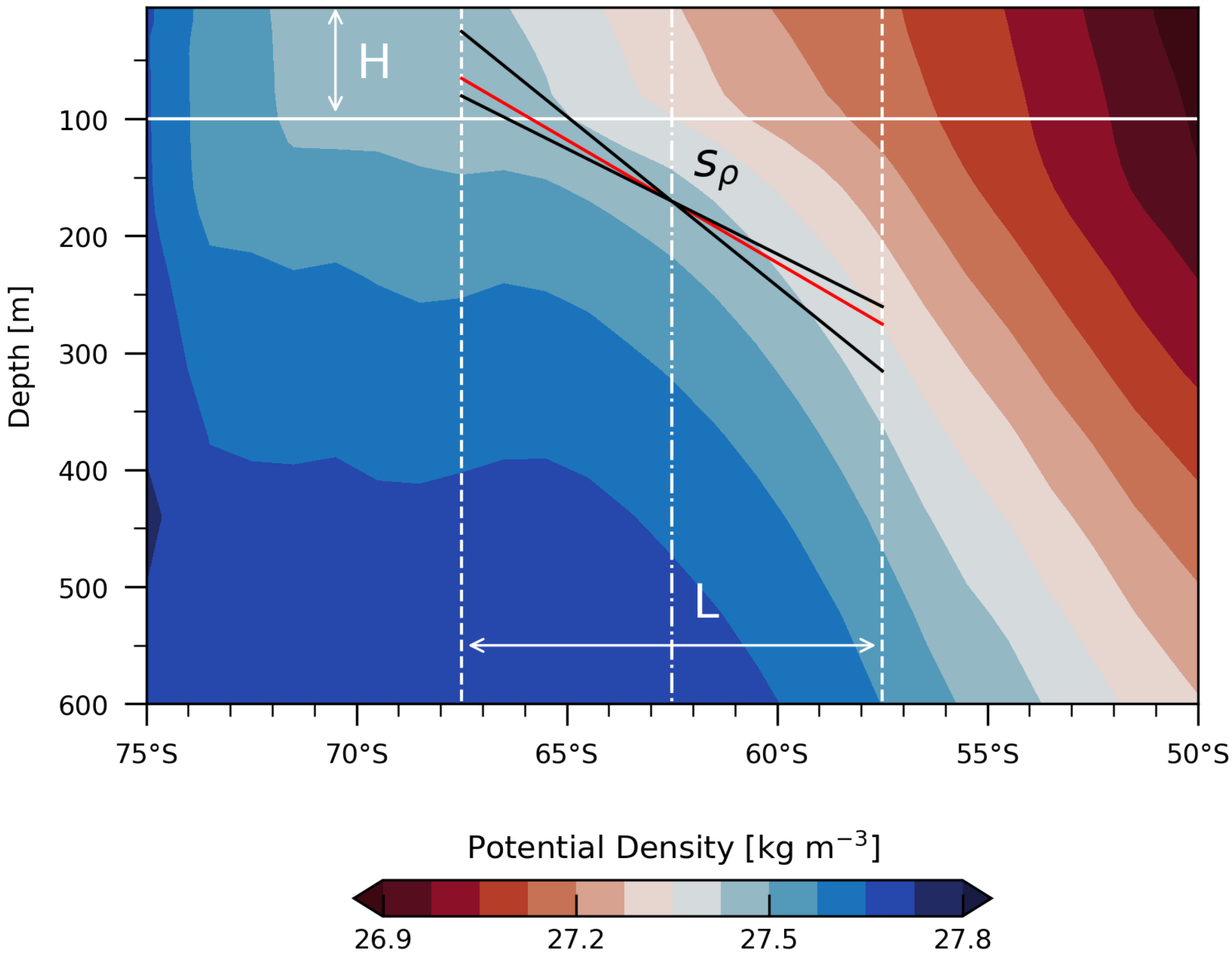

Fig. S7. Slope of mean buoyancy surfaces. Vertical cross-section of climatological spring ocean potential density (color; kg m^{-3}). s_ρ represents the slope of mean buoyancy surfaces, ranging from 0.21×10^{-3} (black line) through 0.30×10^{-3} (red line) to 0.33×10^{-3} (black line). H is depth of the diabatic mesoscale layer. L is approximately 10° latitude, representing the meridional scale of eddy-driven $\Psi^{*'}$.

Table S1. Parameters assumed in the AR(1) model.

Number	Description
$H \approx$ 100 m	Depth of the diabatic mesoscale layer
$K^\dagger \approx$ 1000 m^2 s^{-1}	Eddy transfer coefficient
$\rho_0 =$ 1035 kg m^{-3}	Mean ocean density
$f = -10^{-4}$ s^{-1}	Coriolis parameter
$L \approx$ 1000 km	Meridional scale of eddy-driven $\Psi^{*'}$
$\tau_0^\dagger \approx$ 0.025 N m^{-2}	Amplitude of anomalous zonal wind stress
$s_\rho^\dagger = -\widetilde{b_y}/\widetilde{b_z} \approx (2.1\sim3.3)\times10^{-4}$	Slope of mean buoyancy surfaces
$\alpha_T = 0.5\times10^{-4}$ ℃$^{-1}$	Thermal expansion coefficient typical of cold water

† indicates estimates based on modeled values typical of the mid-latitude Southern Ocean.

References

1. M Kelley, et al., GISS-E2.1: Configurations and climatology. *J. Adv. Model. Earth Syst.* **12**, e2019MS002025 (2020).
2. GL Russell, JR Miller, D Rind, A coupled atmosphere-ocean model for transient climate change studies. *Atmosphere-Ocean* **33**, 683–730 (1995).
3. WG Large, JC McWilliams, SC Doney, Oceanic vertical mixing: A review and a model with a nonlocal boundary layer parameterization. *Rev. Geophys.* **32**, 363–403 (1994).
4. PR Gent, J Willebrand, TJ McDougall, JC McWilliams, Parameterizing eddy-induced tracer transports in ocean circulation models. *J. Phys. Oceanogr.* **25**, 463–474 (1995).
5. M Visbeck, J Marshall, T Haine, M Spall, Specification of eddy transfer coefficients in coarse-resolution ocean circulation models. *J. Phys. Oceanogr.* **27**, 381–402 (1997).
6. J Marshall, JR Scott, A Romanou, M Kelley, A Leboissetier, The dependence of the ocean's MOC on mesoscale eddy diffusivities: A model study. *Ocean. Model.* **111**, 1–8 (2017).
7. SR Jayne, The impact of abyssal mixing parameterizations in an ocean general circulation model. *J. Phys. Oceanogr.* **39**, 1756–1775 (2009).
8. MJ Prather, Numerical advection by conservation of second-order moments. *J. Geophys. Res. Atmospheres* **91**, 6671–6681 (1986).
9. J Zhang, D Rothrock, Modeling Arctic sea ice with an efficient plastic solution. *J. Geophys. Res. Ocean.* **105**, 3325–3338 (2000).
10. CM Bitz, WH Lipscomb, An energy-conserving thermodynamic model of sea ice. *J. Geophys. Res. Ocean.* **104**, 15669–15677 (1999).
11. LM Polvani, KL Smith, Can natural variability explain observed Antarctic sea ice trends? New modeling evidence from CMIP5. *Geophys. Res. Lett.* **40**, 3195–3199 (2013).